JOURNAL OF PROPULSION AND POWER
Vol. 22, No. 1, January–February 2006

Performance Prediction of a Novel Solid-Propellant Microthruster

K. L. Zhang* and S. K. Chou†
National University of Singapore, Singapore 119260, Republic of Singapore
and
S. S. Ang‡
University of Arkansas, Fayetteville, Arkansas 72701

A novel microelectromechanical-systems-based solid-propellant microthruster is developed for stationkeeping, attitude control, drag compensation, and orbit adjust of microspacecraft. Key to the development of the solid-propellant microthruster is the generation of extremely accurate thrust levels and impulse bits. Modeling and simulation can predict the propellant combustion and gas expansion processes inside the microthruster and then derive the microthruster performance. A computational-fluid-dynamics-based model is proposed in this paper to optimize the design by computing the subsonic/supersonic micronozzle flow and calculating the microthruster performance. Wall heat loss and boundary-layer effects, which are especially important for microscale thrusters, are highlighted in the model. Different solid propellants, microthruster geometries, and operating conditions are also evaluated. The computational-fluid-dynamics modeling results are compared with the one-dimensional thermodynamic modeling results and experimental testing data.

Nomenclature

A_c	=	chamber area, m^2
A_e	=	nozzle-exit area, m^2
A_t	=	nozzle-throat area, m^2
a	=	temperature coefficient, $kg^{-n}m^{n+1}s^{2n-1}$
C_p	=	propellant heat capacity, J/kgK
c_e	=	nozzle-exit velocity, m/s
E	=	total energy, J
F	=	force, N
I_t	=	total impulse, Ns
J	=	diffusion flux, kg/m^2s
Kn	=	Knudsen number
k	=	thermal conductivity, W/mK
Ma	=	Mach number
$\dot{m}$	=	mass flow rate, kg/s
n	=	combustion index
p_a	=	ambient pressure, Pa
p_c	=	chamber pressure, Pa
p_e	=	nozzle-exit pressure, Pa
Re	=	Reynolds number
$r = ap_c^n$	=	combustion rate, m/s
S	=	source term
T	=	thrust, N
T_c	=	combustion temperature, K
t	=	time, s
u	=	x velocity in Cartesian coordinates, m/s
v	=	y velocity in Cartesian coordinates, m/s
W_c	=	chamber width, m
W_e	=	nozzle-exit width, m
W_t	=	nozzle-throat width, m
α	=	half-divergence angle, deg
γ	=	thermal capacity ratio
λ	=	mean free path, m
μ	=	viscosity, kg/ms
ρ	=	density, kg/m^3
σ	=	surface tension, kg/m
σ_V	=	accommodation coefficient
τ	=	stress tensor, N/m^2
υ	=	specific volume, m^3/kg

Received 5 December 2003; revision received 6 October 2004; accepted for publication 14 November 2004.

*Research Fellow, Micro Systems Technology Initiative (MSTI), Department of Mechanical Engineering, National University of Singapore, Singapore 119260; kaili_zhang@hotmail.com.

†Professor, Department of Mechanical Engineering, National University of Singapore, Singapore 119260; mpecsk@nus.edu.sg.

‡Professor, Department of Electrical Engineering, University of Arkansas, Fayetteville, AR 72701, USA; ssa@engr.uark.edu.

I. Introduction

MICROELECTROMECHANICAL-SYSTEMS (MEMS)-based smart microspacecraft is an active research field. The cheap, reliable, and versatile clusters of microspacecraft have more advantages than a conventional spacecraft in fabrication, launch, and operation. A micropropulsion system is required in microspacecraft for high-accuracy stationkeeping, attitude control, drag compensation, and orbit adjust. The solid-propellant microthruster is a relatively new class of micropropulsion system. It requires no elaborate system of pumps and valves. Therefore, the total system complexity is minimized. Integrated with MEMS technology, the solid-propellant microthruster has great potential for application in microspacecraft.[1–5] A new solid-propellant microthruster design is advanced here. The proposed solid-propellant microthruster configuration has no pumps, fuel lines, and valves; therefore, there are no moving parts, and the leakage possibility of the propellant is very low.

In the design, a silicon layer is fabricated using deep reactive ion etching (DRIE) to contain a combustion chamber, a convergent-divergent nozzle, and an ignition slot.[6] A Pyrex-7740 glass layer is diced with the same dimensions as the silicon layer and is bonded together with the silicon layer with anodic bonding to form a three-dimensional microthruster. The reason to employ Pyrex-7740 is that its thermal expansion matches that of silicon; it has well characterized and understood methods of anodic bonding to silicon and high electrical resistivity. The chamber is then loaded with the solid propellant. Once ignited, the resultant gas expands through the nozzle, thus producing the desired thrust and impulse bit. The schematic view of a single microthruster is illustrated in Fig. 1. The fabricated three-dimensional microthruster with igniter and solid propellant is shown in Fig. 2.

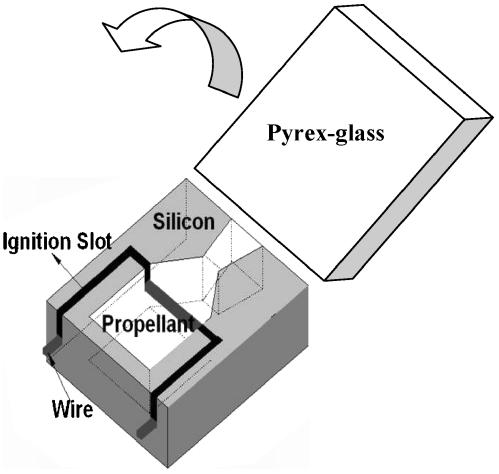

Fig. 1 Schematic of a single microthruster.

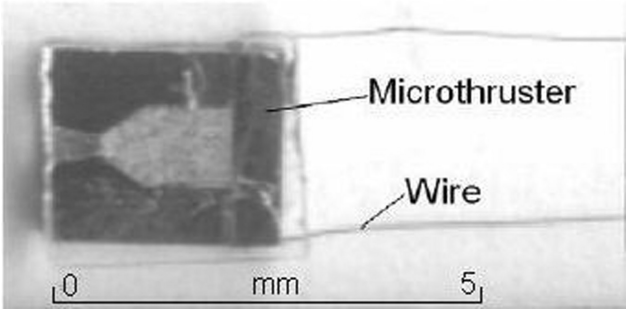

Fig. 2 Microthruster with igniter and propellant.

One of the challenges in developing the solid-propellant microthruster is finding the proper modeling approach to understand and describe the propellant combustion and gas expansion processes inside the microthruster and then derive the microthruster performance. Once the microthruster performance is predicted, the optimal design parameters can be determined. Some modeling techniques for microthrusters have been presented before.[4,7–10] All of the approaches have their own advantages, especially for their specified microthruster designs. However, the convergent-divergent micronozzle jet flow is seldom discussed in detail, which is essential to our novel microthruster. Moreover, the produced impulse bit and the expected performance in space are sometimes missing, which are usually important to spacecraft designers. Furthermore, some interesting phenomena appearing in microscale devices are sometimes ignored. First, the microcombustion in small volume microthruster is somewhat different from normal combustion in conventional thruster. One key difference is the flame quenching problem. The increased surface-area-to-volume ratio that comes with the small size of the microthruster can cause heat loss through the combustor wall to outweigh the heat generated by combustion process. The flame can be extinguished because there is insufficient energy to sustain combustion in the face of heat loss through the microthruster wall. Second, the wall boundary-layer growth can impact the subsonic/supersonic flow in the diverging section of the nozzle. Especially for microscale nozzle flow, the rarefaction effects are suspected to play an important role. Therefore, the microthruster performance variation caused by the micronozzle wall boundary-layer effects should be evaluated.

In this paper, a computational-fluid-dynamics (CFD)-based model is proposed to simulate the propellant microcombustion inside the chamber, calculate the gas flow characteristics through the convergent-divergent micronozzle, predict the produced thrust and impulse bit, and establish a benchmark for the optimum design. The propellant microcombustion, convergent-divergent micronozzle jet flow, heat loss through the wall, slip wall boundary condition, thrust and impulse bit both at sea level and in space, different propellants and diverse microthruster geometries are all addressed in the model.

II. One-Dimensional Thermodynamic Computation

Thermodynamic descriptions of the processes inside the microthruster chamber and convergent-divergent nozzle furnish the mathematical tools needed to calculate the performance and determine the key design parameters of the microthruster system. With proper assumptions and simplifications, the one-dimensional thermodynamic model is adequate for obtaining useful solutions to the microthruster system. The one-dimensional thermodynamic descriptions are usually used to emphasize the importance of exit-to-throat-area ratio and exit-to-chamber-pressure ratio in determining some important parameters, such as exit Mach number and thrust.

The exit-to-chamber-pressure ratio p_e/p_c is an important parameter to identify the gas expansion process through the microthruster nozzle, which can be obtained from Eq. (1) developed by the one-dimensional thermodynamic model.[11]

$$\frac{A_t}{A_e} = \left(\frac{\gamma+1}{2}\right)^{1/(\gamma-1)} \left(\frac{p_e}{p_c}\right)^{1/\gamma} \sqrt{\frac{\gamma+1}{\gamma-1}\left[1-\left(\frac{p_e}{p_c}\right)^{(\gamma-1)/\gamma}\right]} \tag{1}$$

The thrust is a key parameter to describe the propulsion performance, which is calculated by Eq. (2) in the one-dimensional thermodynamic model.[11]

$$T = A_t p_c \sqrt{\frac{2\gamma^2}{\gamma-1}\left(\frac{2}{\gamma+1}\right)^{(\gamma+1)/(\gamma-1)}\left[1-\left(\frac{p_e}{p_c}\right)^{(\gamma-1)/\gamma}\right]} + (p_e - p_a)A_e \tag{2}$$

The results from one-dimensional thermodynamic computation are compared with those of the following two-dimensional CFD modeling to verify the accuracy and advantages of the two-dimensional CFD modeling.

III. Two-Dimensional CFD Modeling

A. Propellant Characteristics

Propellant characteristics affect the microthruster performance in terms of thrust and impulse bit. To achieve the smallest overall structure while preserving relatively high specific impulse, the propellant must be selected carefully. Some representative operational solid propellants are chosen for the microthruster modeling. Their characteristics are listed in Table 1, and the γ value of combustion gas for all listed propellants is assumed to be 1.3 (Ref. 11).

The classical law (3) is used to determine the burning rate for the noncorrosive combustion of the propellant[11]

$$r = ap_c^n \tag{3}$$

where r is the burning rate that is defined as the spatial rate of change of the burning surface normal to the propellant surface and

Table 1 Characteristics of the solid propellants

Solid propellant	a, $\mathrm{kg}^{-n}\mathrm{m}^{n+1}\mathrm{s}^{2n-1}$	n	ρ_P, kg/m^3	Combustion temperature, K
HTPB/AP/Al[a]	6.73×10^{-5}	0.40	1854.6	2000
AN/Polymer[b]	1.51×10^{-6}	0.60	1467.0	900
PU/AP/Al[c]	9.02×10^{-4}	0.15	1771.5	2000
DB[d]	4.00×10^{-5}	0.30	1605.4	1480
DB/AP/Al	5.05×10^{-5}	0.40	1800.0	2250

[a]HTPB, hydroxyl-terminated polybutadiene; AP, ammonium perchlorate; Al, aluminum.
[b]AN, ammonium perchlorate.
[c]PU, polyurethane.
[d]DB, double-base (main ingredients: nitrocellulose and nitroglycerine).

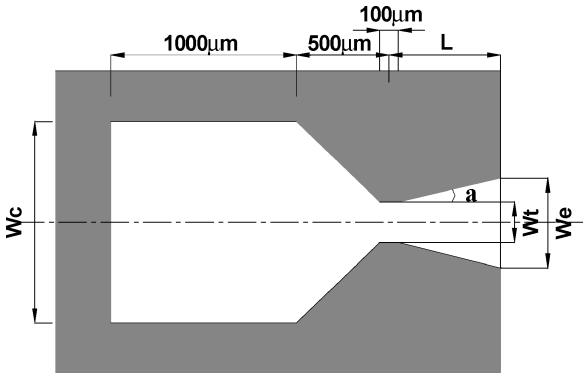

Fig. 3 Geometry of the solid-propellant microthruster.

a (temperature coefficient) is an empirical constant influenced by the initial propellant grain temperature. The rate exponent n, called the combustion index, is independent of the initial propellant grain temperature and describes the effect of chamber pressure on the burning rate.

B. Microthruster Geometry

The dimensions of the simulated microthruster for the present study are shown in Fig. 3. The thickness of the silicon wafer processed here is 650 μm. The silicon in the defined area of the wafer is etched away slowly from the wafer surface. Finally, a deep trench is formed in the wafer with the desired top-view shape and desired depth of 350 μm (see Figs. 1 and 3). The 100-μm plane in the nozzle throat is to avoid sharp edges and facilitate the fabrication. Furthermore, the microthruster has different half-divergence angle α, divergence length L, and widths for the combustion chamber W_c, micronozzle throat W_t, and micronozzle exit W_e. We thus have different chamber-to-throat A_c/A_t and exit-to-throat A_e/A_t area ratios. In the present design, the chamber and nozzle are made by DRIE. Because the DRIE process creates the common etch depth for various features, the chamber and nozzle have the same depth of 350 μm. Consequently, A_c/A_t equals W_c/W_t and A_e/A_t equals W_e/W_t.

C. Governing Equations

The mass conservation equation in Cartesian coordinates can be written as

$$\frac{\partial \rho}{\partial t} + \frac{\partial}{\partial x}(\rho u) + \frac{\partial}{\partial y}(\rho v) = S_m \tag{4}$$

where the source term S_m denotes the mass added to the domain.

The momentum conservation equations can be expressed as

$$\frac{\partial}{\partial t}(\rho u) + \frac{\partial}{\partial x}(\rho u u) + \frac{\partial}{\partial y}(\rho u v) = -\frac{\partial p}{\partial x} + \frac{\partial \tau_{xx}}{\partial x} + \frac{\partial \tau_{yx}}{\partial y} + F_x \tag{5}$$

$$\frac{\partial}{\partial t}(\rho v) + \frac{\partial}{\partial x}(\rho v u) + \frac{\partial}{\partial y}(\rho v v) = -\frac{\partial p}{\partial y} + \frac{\partial \tau_{xy}}{\partial x} + \frac{\partial \tau_{yy}}{\partial y} + F_y \tag{6}$$

where p is the pressure, τ_{ij} are components of the stress tensor, and F_i are the gravity and body forces in the component directions. The stress tensor τ_{ij} is defined as

$$\tau_{ij} = \left[\mu\left(\frac{\partial u_i}{\partial x_j} + \frac{\partial u_j}{\partial x_i}\right)\right] - \frac{2}{3}\mu\frac{\partial u_l}{\partial x_l}\delta_{ij} \tag{7}$$

Finally, the energy conservation equation is written as

$$\frac{\partial}{\partial t}(\rho E) + \frac{\partial}{\partial x_i}[u_i(\rho E + p)] = \frac{\partial}{\partial x_i}\left(k\frac{\partial T}{\partial x_i} - \sum_j h_j J_j + u_j \tau_{ij}\right) + S_h \tag{8}$$

Table 2 Air characteristics at different altitudes

Altitude	Temperature, K	Pressure, atm	Density, kg/m^3
Sea level	300	1	1.2250
50 km	270.65	7.8735×10^{-4}	1.0269×10^{-3}
100 km	195.08	3.1593×10^{-7}	5.6040×10^{-7}

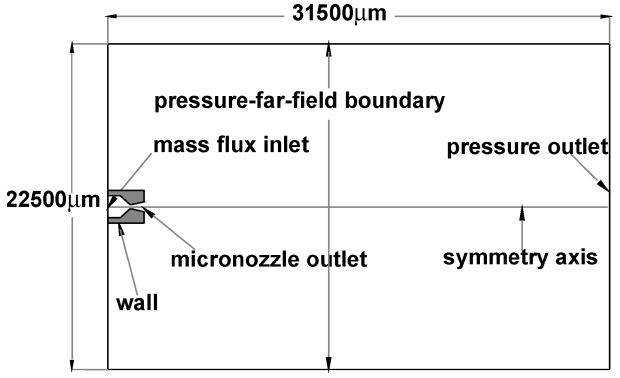

Fig. 4 Computational domain and boundary conditions.

where J_j is the diffusion flux of species j and x_i denotes summation over $i = 1, 2$. The source term S_h denotes heat of chemical reaction and any other volumetric heat sources.

D. Boundary Conditions

The computational domain should extend well beyond the microthruster itself, so that the domain boundary will not influence the problem unrealistically. Figure 4 shows the computational domain and the boundary conditions for the microthruster model. The computational domain is 15 times larger than the microthruster itself.

1. *Inlet Condition*

The combustion of the propellant is combined into the model as the inlet boundary condition. It is assumed that the pressure and temperature conditions in the combustion chamber are homogeneous. The species created from propellant combustion are all gaseous. The chamber temperatures for different propellants in the steady state are shown in Table 1. Because the chamber temperatures are high, all of the combustion gases are well above their respective saturation conditions and follow the perfect-gas law very closely. The micronozzle entrance (base) consists of the burning solid propellant with a surface burning rate per unit area given by

$$\dot{m}/A_c = \rho_p r = \rho_p a P_c^n \tag{9}$$

2. *Wall Conditions*

The wall is made of silicon. The silicon properties are as follows: thermal conductivity = 141.2 W/mk; density = 2330 kg/m^3; and heat capacity = 700 J/kgK. Heat flux through the wall at the inlet is assumed to be zero. All other walls are set to be two-sided walls, so that fluid regions exist on one side and solid regions exist on the other side of these walls. The two-sided walls have coupled thermal and slip boundary conditions.

3. *Outlet, Far-Field, and Initial Conditions*

The outlet, far-field, and initial conditions are as follows: static air; $\mu = 1.7894 \times 10^{-5}$ kg/ms; and $k = 0.0242$ W/mK. The air temperature, pressure, and density are different at varied altitudes as shown in Table 2 (Ref. 11). For reasons described next, most of our simulations are performed for the 50-km condition in this paper.

E. Thrust and Total Impulse Determination

Subsequent to combustion of the propellant, the expansion of the gas through the nozzle produces a thrust T and a total impulse I_t.

The expression for thrust T is given as

$$T = \dot{m}c_e + (p_e - p_a)A_e \tag{10}$$

The values of c_e and p_e are obtained by averaging the integration of velocity and pressure along the nozzle exit. Total impulse I_t is another important parameter to describe the propulsion performance. I_t is the thrust T integrated over the burning time t.

$$I_t = \int_0^t T \, \mathrm{d}t \tag{11}$$

For steady state, thrust T is constant. The burning time is a function of chamber length and burning rate. The chamber length is 1 mm for the designed microthrusters. The burning rate r is calculated from $r = ap_c^n$, where chamber pressure p_c is obtained from the simulation.

IV. Computation

Across the defined computational domain, the Navier–Stokes (N-S) equations are solved using a finite element software-FLUENT®,[§] which has been experimentally validated as a powerful CFD code for solving microcombustion and microflow problems.[12] FLUENT allows users to apply boundary conditions as user-defined functions. Both the inlet boundary condition and the slip-flow wall boundary condition are programmed in C language and inserted into FLUENT as user-defined functions. The computational grids used for the numerical simulations are determined by performing grid-independent study to minimize the modeling error. When the change in the solution between subsequent stages of grid refinement is considered to be negligible, the lower, but still sufficient, grid resolution is kept. The domain is meshed using 7995 nodes. A high grid density is used near the nozzle walls, throat, and exit to resolve the boundary layers and capture the possible shocks and expansion waves. Figure 5 shows the typical computational grid for the domain illustrated in Fig. 4. The enlarged view of the grid in the nozzle is shown in Fig. 6.

For the initial simulations, both laminar and turbulent flow modeling are performed for the microthruster. The resulting flow Reynolds number is below 1500. Therefore, the laminar flow modeling is safely employed for the following simulations. A three-dimensional simulation would provide a complete picture of the flow and an accurate performance prediction. However, this will come at a high computational price. A two-dimensional simulation will provide an accurate performance prediction for our cases in which the endwall boundary layers are thin with respect to the trench depth. The endwalls are the upper and bottom walls of the microthruster. The computational results for steady state are shown in following sections.

A. Effect of Propellant Characteristics on Microthruster Performance

Figure 7 shows the variation of the thrust in space (50 km) with different propellants for the microthrusters with different A_c/A_t ratios with $W_c = 1000$ μm, a half-divergence angle $\alpha = 12$ deg, and a divergence length $L = 600$ μm. The wall heat loss and slip flow are considered in the simulation. It can be clearly seen from Fig. 7 that the influence of the propellant characteristics on the microthruster performance is of great importance. The performance difference of different propellants is mainly caused by the temperature coefficient, combustion index, and combustion temperature variance. Therefore, the propellant should be selected carefully according to the requirements and applications. HTPB/AP/Al is the most common composite propellant today. It has many advantages, such as widest ambient temperature, good burn-rate control, usually stable combustion, good storage stability, good physical properties, and good experience. Therefore, HTPB/AP/Al is selected as the representative for the following simulations.

[§]Data available online at http://www.fluent.com [cited 2003].

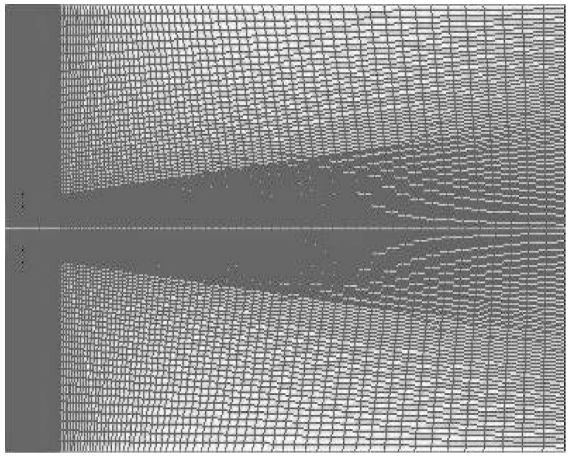

Fig. 5 Computational grid of the domain.

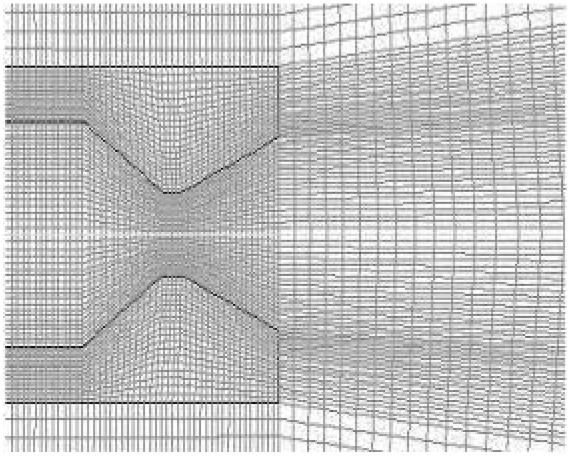

Fig. 6 Enlarged view of the grid in nozzle part.

B. Effect of the Altitude on Microthruster Performance

Microthruster performance is evaluated at sea level, 50 km, and 100 km. Figure 8 shows the thrust and total impulse at different altitudes for microthrusters with different A_c/A_t ratios with $W_c = 1000$ μm, a half-divergence angle $\alpha = 12$ deg, and a divergence length $L = 600$ μm. It can be seen that the thrust and total impulse increase with altitude, though the difference between 50 and 100 km is quite small compared to that with sea level. At sea level, the jet is subsonic, whereas at both 50 and 100 km it is supersonic and nearly identical. Thus, we can use results from 50 km to simulate microthruster performance in space. This approach facilitates comparison of numerical and experimental results because the pressure at 50 km (80 Pa) is much easier to achieve in the laboratory than the pressure at 100 km (0.032 Pa).

C. Effect of Wall Heat Loss on Microthruster Performance

Unlike conventional rocket, the increased surface-area-to-volume ratio that comes with the small size of the microscale thruster can cause the heat loss through the plenum wall to outweigh the heat generated by combustion process, thus resulting in flame quenching. Therefore, the viability of the microthruster should be proven with regard to wall heat loss. To characterize the effect of wall heat loss on microthruster performance, the performance for zero thermal resistance wall, silicon wall, and adiabatic wall are compared. Figure 9 shows the effect of wall conditions on the thrust and total impulse at sea level for the microthrusters with different chamber-to-throat-area ratios A_c/A_t with $W_c = 1000$ μm, a half divergence angle $\alpha = 12$ deg, and a divergence length $L = 600$ μm. It can be seen that the thrust and total impulse for an adiabatic wall are higher than those of zero thermal resistance wall and silicon wall. The reason is that the thermal loss through the wall is

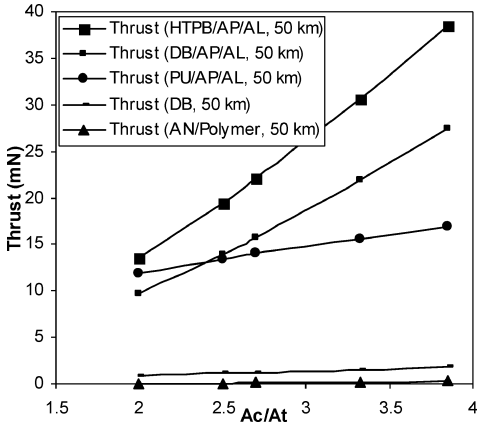

Fig. 7 Thrust variation with propellants and A_c/A_t ratio.

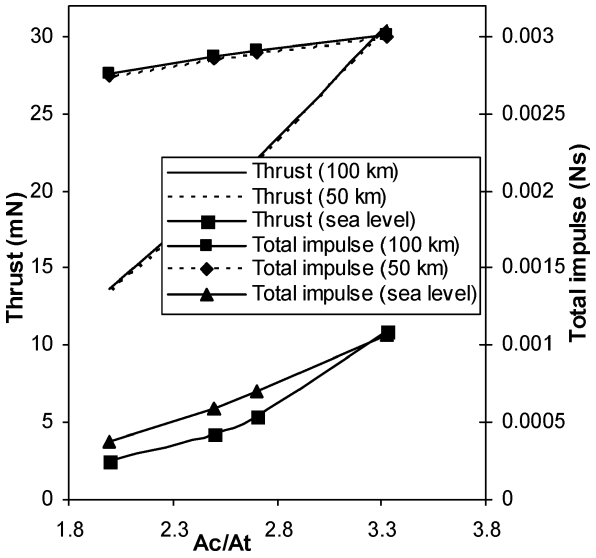

Fig. 8 Thrust and total impulse variations with altitude.

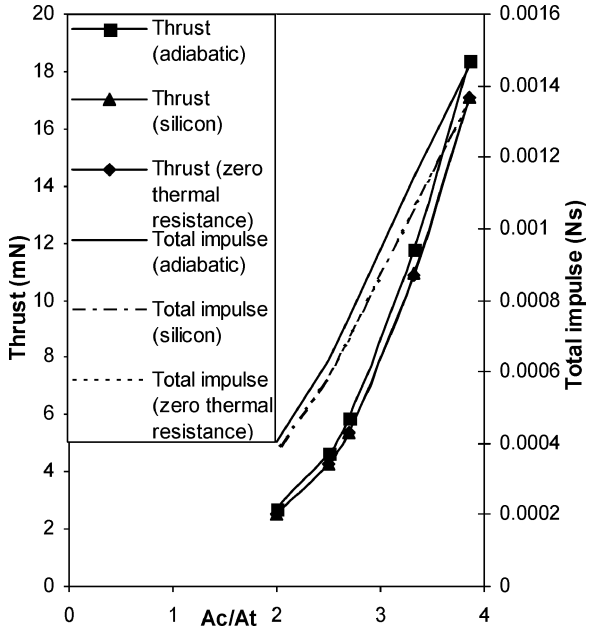

Fig. 9 Effect of wall heat loss on microthruster performance.

neglected if the microthruster wall is assumed to be adiabatic. However, the thrust for zero thermal resistance wall and silicon wall are almost the same. This is because of the high thermal conductivity of silicon compared to the combustion gas and ambient air. The performance losses caused by wall heat loss are $7\sim9$ and $5\sim7\%$ in terms of thrust and total impulse, respectively. The results agree with the previous research performed by Mirels.[7] In that study, the impulse losses were about 10% or less for millimeter-scale thrusters that used high flame speed propellants. The microthruster appears to viable with regard to wall heat loss. Nevertheless, the heat loss through the wall should be considered in the simulation for accurate performance prediction.

D. Effect of Slip Wall Boundary Layer on Microthruster Performance

One key difference between gas flow at microscale and in the macrodomain is the rarefaction effect. When the gas rarefaction effect becomes important, the continuum hypothesis in the macrodomain can be unreasonable. Because the fabricated microthruster dimensions are small with a minimum nozzle feature of 100 μm, the gas rarefaction effect for the device should be tested. Knudsen number Kn, the ratio of mean free path λ to a characteristic length scale of the system, is used to describe various flow regimes. Knudsen number can be written in terms of Mach number (the ratio of the gas velocity to the sound speed) and Reynolds number as $\sqrt{(\pi\gamma/2)}(Ma/Re)$ (Ref. 13). By computing the values of Kn throughout the flowfield at the normal wall boundary condition of noslip, it is found that Kn is between 0.001 and 0.1. For example, the throat Kn is $0.0102\sim0.0155$ at sea level and 0.0028 in space (50 km) for the microthruster with $W_c = 1000$ μm, $W_t = 370$ μm, a half-divergence angle $\alpha = 12$ deg, and a divergence length $L = 600$ μm. This suggests that the gas flow is in the slip regime. In the slip regime the flow is governed by the N-S equations, and rarefaction effect is modeled through the partial slip at the wall using Maxwell's velocity slip condition. Therefore, the wall velocity, which is previously assumed to be zero in the state vector, can be replaced by the term $[(2-\sigma_V)/\sigma_V]Kn(\mathrm{d}u/\mathrm{d}y)_W$, where σ_V is the accommodation coefficient, defined as the fraction of molecules undergoing diffuse reflection, which is assumed to be one as a result of higher microthruster wall roughness.[13]

To demonstrate and qualify the impact of the slip wall boundary layer on microthruster performance, the simulation is performed for the microthrusters with different divergence lengths with $W_c = 1000$ μm, $W_t = 370$ μm, and a half-divergence angle $\alpha = 12$ deg. Figure 10 shows the thrust and total impulse differences for nonslip and slip wall conditions in space (50 km). In the former simulations performed by other researchers, the gas rarefaction effect is normally ignored in the divergent part. This assumption is reasonable for short divergence length. However, the rarefaction

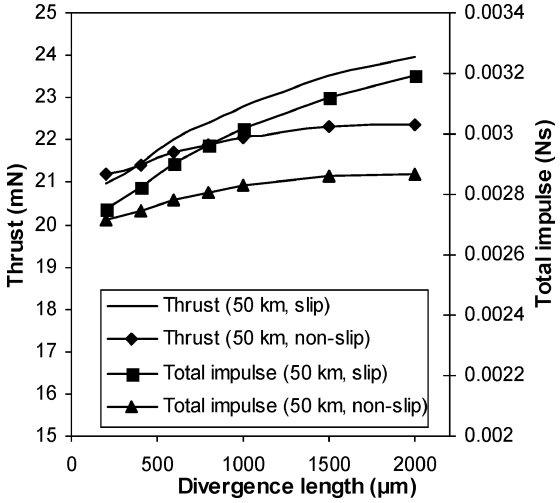

Fig. 10 Effect of slip wall boundary layer on microthruster performance.

effect or wall slip velocity must be considered for long divergence length. It can be clearly seen from Fig. 10 that the differences are small when the divergence length is shorter than 500 μm in our design. When the divergence length is longer than 500 μm, the differences become large and up to 7.2 and 11.3% for thrust and total impulse, respectively. Therefore, the wall slip flow cannot be neglected for microscale thrusters. Accordingly, the wall slip flow will be considered in the following simulations.

E. Effect of Exit-to-Throat-Area Ratio on Microthruster Performance

The exit-to-throat-area ratio A_e/A_t of the nozzle is a major driver of microthruster performance. To illustrate and qualify the impact of A_e/A_t on the thrust and impulse, the gas flow is computed for the microthrusters with different A_e/A_t and $W_c = 1000\,\mu$m, $W_t = 370\,\mu$m, and a divergence length $L = 600\,\mu$m. Figure 11 shows the thrust and total impulse variations with A_e/A_t. At sea level, when A_e/A_t increases, the thrust and total impulse decrease slowly and tend to become stable around 2.45 mN and 3.13×10^{-4} N · s, respectively, for $A_e/A_t > 3.0$. All of the designed nozzles are overexpanded because of the higher ambient pressure at sea level. When $A_e/A_t > 1.85$, separation of the flow takes place inside the divergent portion of the nozzle as shown in Fig. 12. In space (50 km), both the thrust and total impulse increase slightly with the increase of A_e/A_t. When A_e/A_t is too small (for $A_e/A_t < 1.63$ in our design), the nozzle is underexpanded. However, when A_e/A_t is too big (for $A_e/A_t > 2.08$ in our design), the nozzle is overexpanded as shown in Fig. 13. In our design, the optimum expansions are achieved at $1.63 < A_e/A_t < 2.08$ in space.

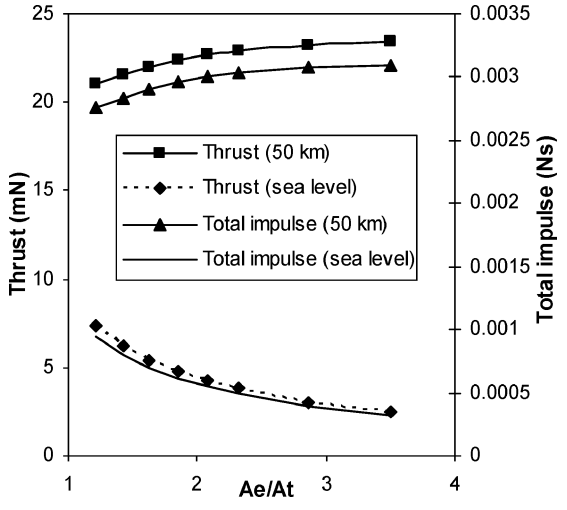

Fig. 11 Thrust and total impulse variations with A_e/A_t ratio.

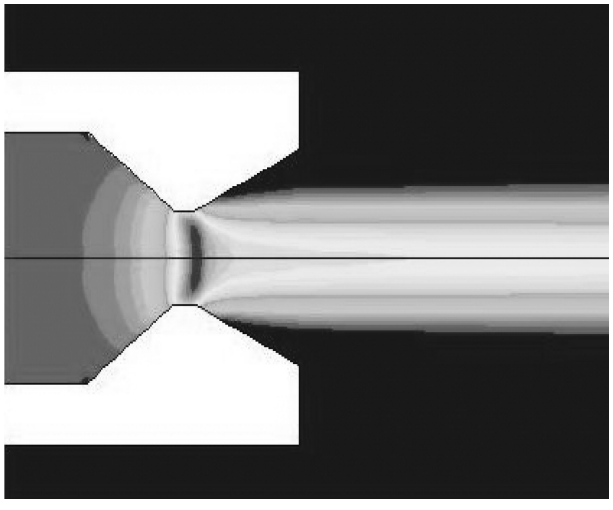

Fig. 12 Flow separation at sea level.

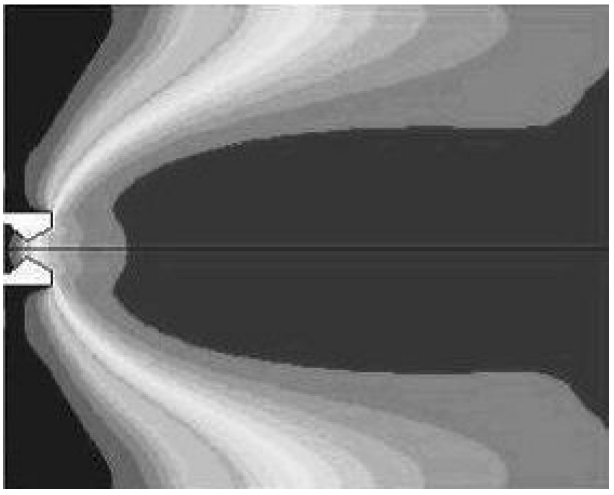

Fig. 13 Overexpanded flow in space.

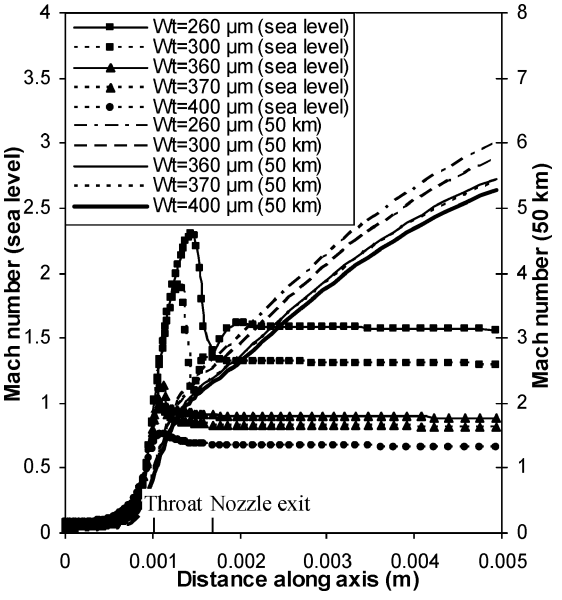

Fig. 14 Mach-number profiles along the axis at different throat widths.

F. Effect of Chamber-to-Throat-Area Ratio on Microthruster Performance

The classical law (3) expresses the fact that the burning rate is dependent on the propellant composition and the chamber pressure. The chamber pressure, however, is determined by the equilibrium that should exist between the gas generation rate and the nozzle exhaust flow rate. Thus the stable pressure level that is achieved is determined by the propellant composition and the ratio between the propellant burning area A_c and the nozzle throat area A_t. Consequently, as far as the nozzle design is concerned, the A_c/A_t ratio is an important parameter that impacts the microthruster performance.

1. Effect of Chamber-to-Throat-Area Ratio on Flow Pattern

Figure 14 shows the Mach-number profiles along the axis at different A_c/A_t ratios for the microthrusters with $W_c = 1000\,\mu$m, a half-divergence angle $\alpha = 12$ deg, and a divergence length $L = 600\,\mu$m. In the abscissa, 0 corresponds to the position inside the chamber 500 μm away from the end of the chamber; 0.001 corresponds to the center of the nozzle throat plane; and 0.0016 corresponds to the nozzle exit. At sea level, when $A_c/A_t = 2.50$ ($W_t = 400\,\mu$m), the

flow through the nozzle is completely subsonic. The flow accelerates out of the chamber through the convergent section, reaching its maximum (subsonic) velocity at the throat. The flow then decelerates through the divergent section and exhausts into the ambient as a subsonic jet. When $A_c/A_t = 2.70$ ($W_t = 370$ μm), the flow pattern is exactly the same as in subsonic flow, except that the flow velocity at the throat has just reached Mach 1. Flow through the nozzle is just choked. When $A_c/A_t = 2.78$ ($W_t = 360$ μm), the Mach number at the throat is still one, but a region of supersonic flow forms just downstream of the throat. Unlike a subsonic flow, the supersonic flow accelerates as the area gets bigger. This region of supersonic acceleration is terminated by a normal shock wave. The shock wave produces a near-instantaneous deceleration of the flow to subsonic velocity. This subsonic flow then decelerates through the remainder of the divergent section and exhausts as a subsonic jet. When $A_c/A_t = 3.33$ ($W_t = 300$ μm) and $A_c/A_t = 3.85$ ($W_t = 260$ μm), the shock bends out into the jet; the jet becomes a supersonic jet. Because the shock is no longer perpendicular to the flow near the nozzle walls, it deflects inward as it leaves the exit producing an initially contracting jet. We refer to this as overexpanded flow because in this case the pressure at the nozzle exit is lower than the ambient pressure. In space, the flow patterns for different A_c/A_t ratios are similar. The flow in the chamber and convergent section is subsonic. Then it reaches sonic flow at the throat (Mach number = 1). In the divergent part, the supersonic flow accelerates when the area gets bigger and exhausts as a supersonic jet.

2. Effect of Chamber-to-Throat-Area Ratio on Thrust and Total Impulse

By increasing the A_c/A_t ratio, the chamber pressure is greatly increased, and the gas can be accelerated to a higher velocity, resulting in a greater thrust level. Figure 15 shows the variations of the thrust and total impulse as a function of A_c/A_t ratio for the microthrusters with $W_c = 1000$ μm, a half-divergence angle $\alpha = 12$ deg, and a divergence length $L = 600$ μm. Both at sea level and in space, the thrust increases when the A_c/A_t ratio increases. The total impulse increases with the increase of A_c/A_t ratio when A_c/A_t ratio is lower than five. However, when A_c/A_t ratio is higher than five, the total impulse changes very slowly although A_c/A_t ratio increases from 5 to 10. The reason is that not only the thrust increases but also the chamber pressure increases when the A_c/A_t ratio increases. The chamber pressure increase causes burning rate to rise, thus resulting in a decrease in burn time. Consequently, as the integration of thrust and burning time, the total impulse changes very slowly. One key to designing an efficient subsonic nozzle lies in adjusting the nozzle throat area in order to have a fluid throat velocity close to the sound speed. For our microthrusters, this is achieved for $A_c/A_t = 2.70$ at sea level. In space, the jet is uniformly supersonic for the A_c/A_t ratios in our design.

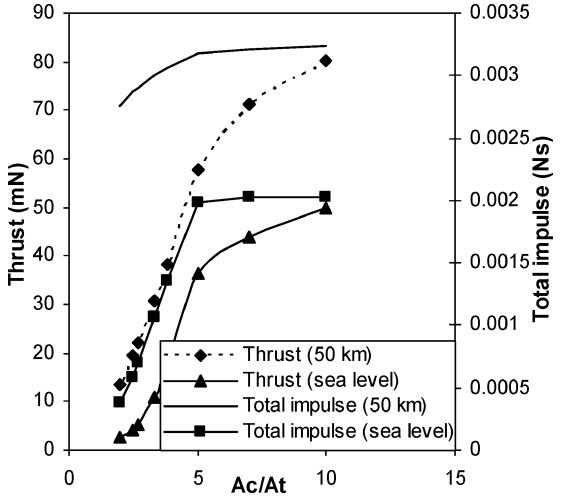

Fig. 15 Thrust and total impulse variations with A_c/A_t ratio.

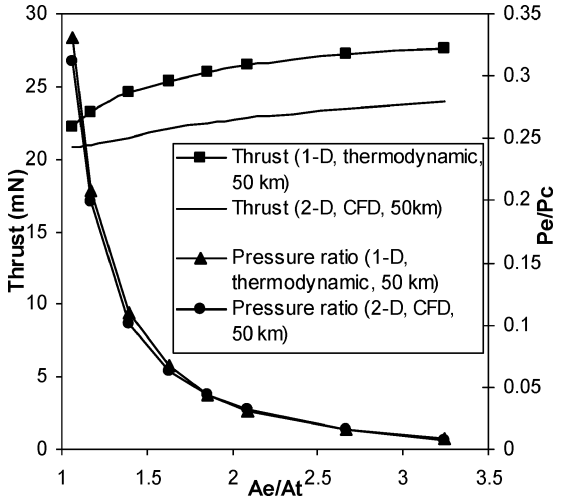

Fig. 16 P_e/P_c ratio and thrust comparisons.

G. Comparison with One-Dimensional Thermodynamic Modeling

Figure 16 shows the p_e/p_c ratios and thrusts obtained from the one-dimensional thermodynamic modeling and two-dimensional CFD modeling, respectively. The simulations are performed for the microthrusters with different A_e/A_t with $W_c = 1000$ μm, a half-divergence angle $\alpha = 12$ deg, and $W_t = 370$ μm. Both the p_e/p_c ratio and thrust from the one-dimensional modeling are higher than those from the two-dimensional modeling. The differences are mainly caused by some of the assumptions and simplifications of the one-dimensional modeling that are somewhat different from actual situations. First, the heat transfer across the walls is ignored in one-dimensional modeling, whereas the decrement in thrust as a result of wall heat loss is about $7 \sim 9\%$ for microthruster according to two-dimensional modeling. Second, the boundary-layer effects are neglected in one-dimensional modeling, whereas slip wall boundary-layer effect is important for microthruster nozzle flow. It can impact the thrust at about 7.2% in accordance with the two-dimensional modeling. Third, the possible discontinuity in the nozzle flow is ignored in one-dimensional modeling, whereas the two-dimensional model shows that flow separation or discontinuity does exit in the nozzle flow. The flow separation decreases the microthruster performance because of the overexpanded nozzle flow. Fourth, the gas velocity, pressure, and temperature are all supposed to be uniform across any section normal to the nozzle axis in one-dimensional modeling, which is obviously not suitable for accurate microthruster performance prediction compared to two-dimensional modeling.

H. Comparison with Experimental Testing Results

A specially designed measurement setup is constructed to characterize the proposed microthruster performance.[14] Figure 17 shows a typical experimental thrust curve using HTPB/AP/Al as the solid propellant. The testing is performed at atmospheric pressure and approximately 300 K. In the thrust curve, a small peak is followed by a steady burn, which is commensurate with what might be expected for an end burning geometry.[15] However, the thrust curve is greatly different from the thrust curve using gunpowder-based solid propellant.[14] This is mainly because of the propellant characteristics difference. Table 3 shows the performance comparison between two-dimensional CFD simulation and experimental testing for two microthrusters with $W_c = 1000$ μm, a half-divergence angle $\alpha = 12$ deg, and a divergence length $L = 600$ μm. The experimental thrust levels are lower than those from simulation. But the total impulses from testing are higher than those from simulation, which is mainly because of the big difference of burning time between testing and simulation. The main cause for the burning time difference is that the unsteady combustion is neglected in the simulation. There are some other possible causes for the performance difference, such as the characteristics variation between the HTPB/AP/Al propellant

Table 3 Performance comparison between two-dimensional simulation and experimental testing

Nozzle throat width	Thrust (two-dimensional)	Thrust (testing)	Burning time (two-dimensional)	Burning time (testing)	Total impulse (two-dimensional)	Total impulse (testing)
$W_t = 400\ \mu$m	4.273 mN	3.698 mN	138 ms	180 ms	0.590 mN · s	0.665 mN · s
Difference	13.457%		23.333%		11.278%	
$W_t = 370\ \mu$m	5.402 mN	4.631 mN	129 ms	169 ms	0.699 mN · s	0.792 mN · s
Difference	14.273%		23.669%		11.742%	

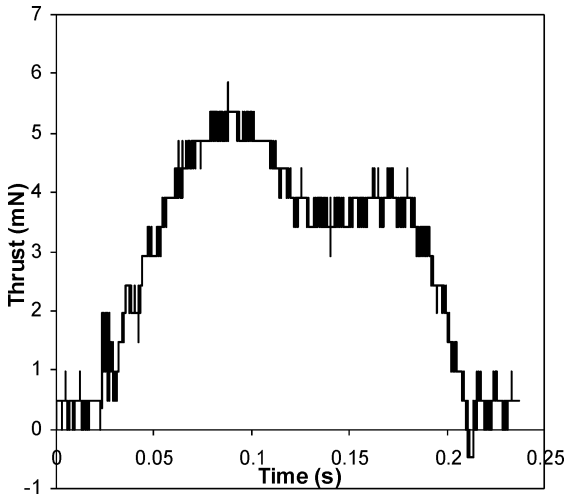

Fig. 17 Typical microthruster thrust curve from experimental testing.

employed here and that from Ref. 11, the testing errors, the nozzle wall roughness, and the heat loss.

V. Conclusions

Computational-fluid-dynamics (CFD)-based simulation is performed for solid-propellant microthrusters. The simulation is carried out to get the optimal microthruster configuration and to predict the performance. The convergent-divergent nozzle jet flow is discussed in detail for microscale thruster. The simulation indicates that chamber-to-throat-area ratio and exit-to-throat-area ratio have great impact on the jet flow patterns. Wall heat-loss effect is important for the viability of microthruster. The simulation shows that wall heat loss can change the microthruster performance by $5 \sim 7\%$ in terms of total impulse. Slip wall boundary layer effect is significant because rarefaction effects play an important role in microthruster. According to the simulation, microthruster total impulse can vary up to 11.3% as a result of slip wall boundary-layer effect. The propellants also have crucial impact on microthruster performance. They must be selected carefully according to the requirements.

The employment of the burning-rate law in the microscale thruster has limitations and needs to be validated for microthrusters. The combustion gases are assumed to follow the perfect-gas law, which should be studied further owing to the aluminum contained in the propellant. Other assumptions made, for example, the assumption of axisymmetric, steady flow must also be questioned to address the difference among two-dimensional CFD simulation, one-dimensional thermodynamic computation, and experimental testing.

Acknowledgments

This work is funded by National University of Singapore (NUS) under Grant R-265-000-150-112. The authors wish to acknowledge the support of the Institute of Materials Research and Engineering, NUS Supercomputing-Visualisation Center, Micro Systems Technology Initiative Lab, Advanced Manufacture Lab, and Thermo Lab for their contributions to the solid-propellant preparation, the microthruster fabrication, and simulation.

References

[1]Youngner, D. W., Lu, S. T., Choueiri, E., Neidert, J. B., Black, R. E., III, Graham, K. J., Fahey, D., Lucus, R., and Zhu, X., "MEMS Mega-Pixel Micro-Thruster Arrays for Small Satellite Stationkeeping," *14th Annual AIAA/USU Conference on Small Satellites*, AIAA, Reston, VA, 2000, pp. 1–8.

[2]Lewis, D. H., Jr., Janson, S. W., Cohen, R. B., and Antonsson, E. K., "Digital Micropropulsion," *Sensors and Actuators A*, Vol. 80, No. 2, 2000, pp. 143–154.

[3]Teasdale, D., Milanovic, V., Chang, P., and Pister, K. S. J., "Microrockets for Smart Dust," *Smart Materials and Structures*, Vol. 10, No. 6, 2001, pp. 1145–1155.

[4]Rossi, C., Do Conto, T., Esteve, D., and Larangot, B., "Design, Fabrication and Modeling of MEMS-Based Microthrusters for Space Application," *Smart Materials and Structures*, Vol. 10, No. 6, 2001, pp. 1156–1162.

[5]Zhang, K. L., Chou, S. K., and Ang, S. S., "MEMS-Based Solid Propellant Microthruster Design, Simulation, Fabrication and Testing," *Journal of Microelectromechanical Systems*, Vol. 13, No. 2, 2004, pp. 165–175.

[6]Menz, W., Mohr, J., and Paul, O., *Microsystem Technology*, Wiley-Vch, Singapore, 2001, pp. 242–245.

[7]Mirels, H., "Effect of Wall on Impulse of Solid Propellant Driven Millimeter-Scale Thrusters," *AIAA Journal*, Vol. 37, No. 12, 1999, pp. 1617–1624.

[8]Bayt, R., and Breuer, K., "Systems Design and Performance of Hot and Cold Supersonic Microjets," AIAA Paper 2001-0721, Jan. 2001.

[9]Orieux, S., Rossi, C., and Esteve, D., "Compact Model Based on a Lumped Parameter Approach for the Prediction of Solid Propellant Microrocket Performance," *Sensors and Actuators A*, Vol. 101, No. 3, 2002, pp. 383–391.

[10]Gatsonis, N. A., Nanson, R. A., and Le Beau, G. J., "Simulations of Cold-Gas Nozzle and Plume Flows and Flight Data Comparisons," *Journal of Spacecraft and Rockets*, Vol. 37, No. 1, 2000, pp. 39–48.

[11]Sutton, G. P., and Biblarz, O., *Rocket Propulsion Elements: an Introduction to the Engineering of Rockets*, Wiley, New York, 2001, pp. 59, 63, 428, 479, 730.

[12]Mehra, A., "Development of a High Power Density Combustion System for a Silicon Micro Gas Turbine Engine," Ph.D. Dissertation, Massachusetts Inst. of Technology, Cambridge, 2000, pp. 141–145.

[13]Karniadakis, G. E., and Beskok, A., *Micro Flows: Fundamentals and Simulation*, Springer-Verlag, New York, 2002, pp. 45–51.

[14]Zhang, K. L., Chou, S. K., and Ang, S. S., "Development of a Solid Propellant Micro-Thruster with Chamber and Nozzle Etched on a Wafer Surface," *Journal of Micromechanics and Microengineering*, Vol. 14, No. 6, 2004, pp. 785–792.

[15]Purrington, G. W., "Plastic Resin Bonded High Energy Rocket Fuel Systems," *Basic Ingredient Study and Small Motor Production*, Vol. III, Firefox Enterprises Inc., Pocatello, ID, 1998–2001, pp. 107–111.